Helmholtz-Zentrum Dresden-Rossendorf (HZDR)

Metallic twin boundaries boost the hydrogen evolution reaction on the basal plane of molybdenum selenotellurides

Metallic twin boundaries and anion substitution boost the hydrogen evolution reaction on the basal plane of molybdenum selenotellurides

Tomasz Kosmala, Horacio Coy Diaz, Hannu-Pekka Komsa, Yujing Ma, Arkady V. Krasheninnikov Matthias Batzill, Stefano Agnoli*

Dr T. Kosmala, Prof. Dr. S. Agnoli
Department of Chemical Sciences and INSTM research unit, University of Padova, 35131
Padova Italy E-mail: stefano.agnoli@unipd.it
Dr. H. C. Diaz, Dr. Y. Ma, Prof. Dr. M. Batzill
Department of Physics, University of South Florida, Tampa, Florida 33620, United States Dr.
H.-P. Komsa, Dr. A. V. Krasheninnikov, Department of Applied Physics, Aalto University,
Aalto, Finland
Dr. A. V. Krasheninnikov Helmholtz-Zentrum Dresden-Rossendorf, Institute of Ion Beam
Physics and Materials Research, Dresden, Germany

Abstract: The hydrogen evolution reaction (HER) is a fundamental process that impacts several

important clean energy technologies. Great efforts have been taken to identify alternative

materials that could replace Pt for this reaction or that may present additional
functional

properties such as optical activity and advanced electronic properties. Herein, it is reported a

comparative study of the HER activity of $MoTe_2$, $MoSe_2$ and for the first time their solid

solutions, obtained as two dimensional ultrathin films on highly oriented pyrolytic graphite.

Combining advanced characterization techniques and density functional theory calculations

with electrochemical measurements, it is shown that the chemical activity of the scarcely reactive 2H phases can be boosted by the presence metallic twin boundaries. These defects, which are thermodynamically stable and naturally present on molecular beam epitaxy grown films, endow the basal plane of the 2H phase with a high chemical activity, such as in the case of the metastable 1T polymorph.

The production of hydrogen from water splitting, using renewable energy sources, is one of the possible strategies to solve the current climate challenges, because hydrogen is a convenient energy carrier that can be used to chemically store the energy produced by other intermittent renewable sources. Electrolysis is the most efficient and industrially scalable method to split water. It comprises two separate reactions: the hydrogen evolution reaction (HER) and the oxygen evolution reaction (OER). The former involves the adsorption and reduction of protons from the electrolyte to molecular hydrogen as a consequence of the application of a sufficiently high potential.[1] To reduce this potential and speed up the kinetics, efficient catalysts are needed. Currently, Pt group metals[2,3] show the highest activities, however their high cost and shortage of supply prevent a widespread industrial application. Among possible alternatives, transition metal carbides, chalcogenides, nitrides and phosphides are particularly promising, considering the good performance and low cost and natural abundance.[4,5]

2

Transition metal chalcogenides (TMC) especially, have kindled a tremendous interest since the edges of MoS_2 nanoparticles exhibit a close resemblance to the catalytic center of the hydrogenase enzyme.[6] Nonetheless in the bulk form, these materials provide poor performances because of the low density of active sites and scarce electrical conductivity. Different strategies were adopted to ameliorate TMCs: electronic conduction can be improved by using metastable polymorphs with metallic behavior such as the 1T phases of WS_2 and MoS_2,[7,8] creating conduction channels exploiting special morphology[9] or through the synthesis of nanocomposites with materials that exhibit superior conduction properties such as graphene[10,11] or gold.[12] On the other hand, the number of active sites may be increased by introducing dopants,[13] defects[14] and vacancies,[15,16] maximizing edge sites,[17,18] or through mechanical strain.[19] So far, most works on TMCs have focused on Mo and W sulfides and selenides, and more recently, sulfides of transition metals such as Ti, V, Ni, Co, Nb and Ta.[20] On the contrary, metal tellurides are scarcely investigated, although their exceptional optical[21] and electronic properties[22,23] are arousing a growing interest. Actually, the combination of the different functional properties spanning from advanced electronic properties and chemical or optical activity is expected to promote the realization of a new generation of multifunctional smart devices.[24,25,26] Unfortunately though, the study of telluride chemistry is still at its infancy and only few papers deal with this subject.[27,28,29] Quite recently, the formation of solid solutions of different TMCs demonstrated to be a powerful method to improve the catalytic activity.[30] Some of the best preforming materials

have been obtained by mixing different TMCs creating sulfoselenides of molybdenum ($MoS_{2-x}Se_x$),[31,32,33] tungsten ($WS_{2-x}Se_x$)[34,35,36] or mixed metal sulfides and selenides, such as $Fe_{1-x}Co_xSe_2$,[37] $Co_xMo_{1-x}Se_2$[38] and Ni-Mo-S alloys.[39]

Herein, we have investigated the HER activity of $MoSe_2$ and $MoTe_2$ and their solid solutions, (i.e. samples S1 ($MoSe_{0.32}Te_{1.68}$) and S2 ($MoSe_{0.12}Te_{1.79}$) using highly controlled model systems prepared by Molecular Beam Epitaxy (MBE).[40,41,42,43] These films have a low surface area and very few morphological defects (edges, holes), so they allow shedding light on the inherent electrochemistry of the basal plane.

Figure 1 reports AFM and STM data of a typical molybdenum selenotelluride (sample S1) 2-3 layer thick film grown by MBE on highly oriented pyrolytic graphite (HOPG) substrates. Details about the sample synthesis and their physical properties and defect structures can be found in ref. [40, 41, 42, 43]. $MoSe_2$, $MoTe_2$ and $MoSe_{2-x}Te_x$ form smooth films made up by large monolayer islands that cover homogeneously the HOPG substrate, and the morphology is the same for all samples regardless of the composition. The ultraviolet photoemission spectrum in Figure 1b shows the valence band maximum at ~0.57 eV below the Fermi-level, which is very similar to $2H$-$MoTe_2$, but strong photoemission features are visible in the band gap, indicating the presence of defect states. The comparison of STM topographies taken with positive (filled states, Figure. 1c (i)) and negative (empty states, Figure 1c (ii)) bias, allows identifying line defects that are characterized by a special electronic contrast, (see the zoomed-in image in Figure 1c (iii)), where the double-line structure in empty state images is due to metal

4

twin boundaries (MTB), as previously reported.[41] STS spectra taken in between (point 'A') and on (point 'B') line defects, suggest the metallic nature of such boundaries, which explains the presence of the intra bandgap states observed in the photoemission valence band spectra. On the other hand, no other type of point defects such as anion vacancies, which should appear as large dark spots[44] have been observed in atomically resolved STM images.

The elemental composition of the TMC thin films was determined by X-ray photoelectron spectroscopy (XPS). The survey spectra of the different samples (see **Figure S1**) show the peaks due to Mo, Te and/or Se, beside the signal due to O 1s due to air exposure. **Figure 2** shows the high-resolution photoemission spectra of Te 3d, Mo 3d and Se 3d before the electrochemical measurements, together with their deconvolution into chemically shifted components. For pure $MoSe_2$, the peaks at binding energy (BE) of 228.7 eV and 231.8 eV correspond to Mo 3d photoemission doublet, while the features at 54.2 eV and 55.1 eV to $Se3d_{5/2}$ and $Se3d_{3/2}$ levels, respectively. These BE positions are typical of Mo^{4+} and Se^{2-} in the $2H-MoSe_2$.[45] A small peak at 232.2 eV indicates the presence (6.4%) of oxidized Mo^{6+} species, (likely MoO_3).[46,47] Concerning the $2H-MoSe_2$ phase, using the integrated areas of Mo 3d and Se 3d photoemission spectra, normalized to sensitivity factors, we obtain a Se/Mo ratio of 1.96. The high-resolution photoemission spectra of the $MoTe_2$/HOPG thin films reveal the presence of the Mo $3d_{5/2}$ peak maximum at 227.8 eV, whereas the Te $3d_{5/2}$ peak maximum is located at 572.8 eV, suggesting the formation of the $2H-MoTe_2$ phase. Partial oxidation due to air

exposure is evidenced by the peaks at 232.2 eV in the Mo $3d_{5/2}$ photoemission line and at 576.5 eV in the Te$3d_{5/2}$ spectrum, which indicate the formation of MoO_3 and TeO_2, respectively.[44,48] In the case mixed $MoSe_{2-x}Te_x$/HOPG films (i.e. sample S1 and S2), the Mo $3d_{5/2}$ (at 227.8 eV), Te $3d_{5/2}$ (at 572.9 eV) and Se $3d_{5/2}$ (at 53.80 eV) peaks are observed at the same BE positions for any value of Se/Te ratio, which are different from BE observed for pure $MoSe_2$. In both selenotellurides, intense peaks associated with surface oxidation are visible in Mo 3d and Te 3d core levels. In the case of sample S2, a mild sputtering treatment (0.5 keV Ar^+, 3 minutes) was performed (i.e. sample S2$_S$) to remove partially the oxide and increase the defect density. After this treatment, the Te 3d photoemission line shows four distinct doublets: one intense component with the Te $3d_{5/2}$ peak centered at 572.9 eV, which is due to the 2H-MoTe$_2$ phase and accounts for 73.8 % of the overall intensity, a small peak due to TeO_2 (1.3 %) with the Te$3d_{5/2}$ peak maximum at 576.5 eV, a TeO_{2-x} sub-oxide component at 574.1 eV (8.3 %)[49] and a peak due to defects (Te $3d_{5/2}$ (def)) at 572.3 eV (16.6 at. %).[45] This latter peak was not present in the pristine sample, indicating the absence of vacancies as confirmed by STM. After sputtering the photoemission spectrum of Mo 3d shows a rather complex shape, and can be deconvoluted in four distinct doublets. The most intense component shows the Mo $3d_{5/2}$ peak maximum at 227.8 eV, ascribed to 2H-$MoSe_{2-x}Te_x$ (64 at. %). A second component with the Mo $3d_{5/2}$ peak maximum at 232.2 eV corresponds to $MoO3$ (8.5 at. %), whereas the last two doublets with the Mo$3d_{5/2}$ peak maxima at 228.9 eV (20.8 at. %) and 230.5 eV (6.7 at. %) are assigned to sub-stochiometric MoO_{3-x} or MoO_2,[47,50] or complex structural configuration such

as "Te-Mo-O bonds". The calculated Te/Mo and Se/Mo ratio of $MoSe_{2-x}Te_x$ after sputtering (taking into account only the chemically shifted components of the 2H phase) are 1.79 and 0.12, respectively, indicating a substantial reduction of Se and partially of Te, (see **Table 1**) indicating the formation of a significant amount of anion vacancies.

The electrochemical activity of the thin films was tested in Ar-saturated 0.5 M H_2SO_4 electrolyte. The polarization curves are shown in **Figure 3a** together with the data of a bare HOPG electrode and a Pt/C commercial catalyst (Johnson Matthey, 20 wt%) on GC electrode, as reference. The onset potential of pure $MoSe_2$ and $MoTe_2$ are -0.29 V and -0.25 V, respectively, whereas the mixed selenotellurides show better performances. The onset potential of S1 is at -0.24 V, while S2, the Te richest selenotelluride, exhibits a value, about -0.19 V vs RHE, which after sputtering slightly improves to -0.18 vs RHE.

In the literature, the most used figure of merit to compare HER performance is the potential needed to achieve a current density of 10 mAcm^{-2}.[51,52] By plotting these values as a function of the film composition (i.e. Se/Mo ratio) we can observe a volcano type behavior. Overall, the best catalytic performance is exhibited by S2 after the sputtering (-0.41V), which has a stoichiometry of $MoSe_{0.12}Te_{1.79}$, followed by pristine S2 (-0.45V) with composition $MoSe_{0.17}Te_{1.83}$, (see **Table 2**). The small increase in the activity after sputtering suggests that the formation of anion vacancies and exposure of metal terminating edges as a consequence of oxide removal is beneficial to the electrochemical activity as reported in other works, but to a limited extent. Therefore, also the basal plane of these materials must be endowed with a high

intrinsic activity. Moreover, pure $MoTe_2$ is clearly more active than pure $MoSe_2$ and the increase of the Te fraction (or conversely reduction of Se) in the selenotellurides is associated with better performances. Nonetheless the presence of a small amount of Se is fundamental to achieve the highest activity. For comparison to produce 10 mA/cm^2, liquid exfoliated nanosheets of 2H-$MoTe_2$, 2H-WTe_2 require comparable, but slightly worse potentials, which are -0.48 V and -0.55 V,[53] respectively, whereas 2H-$MoSe_2$ and 1T-$MoSe_2$ a potential of about -0.29 V. However, it has to be noted that these data were obtained on high surface area materials with an active phase loading of about 0.1-1 mg/cm^2. In our case, we purposely used very flat ultrathin films with a very low coverage (~1$\mu g/cm^2$) and surface are in order to maximize the sensitivity toward the basal plane only.

To improve our understanding of the electrochemical properties of the sample and to determine the reaction mechanism of the HER, we have carried out a Tafel analysis (see Supporting Information for details). Figure 3b and Table 2 show the Tafel slope values obtained for the samples, together with those of HOPG and Pt/C. The highest catalytic activity is displayed by sample S2 with a Tafel slope of 64 mV/dec, which slightly improves to 62 mV/dec after sputtering. On the contrary, sample S1 and $MoSe_2$, show larger Tafel slopes of 94 mV/dec and 115 mV/dec, respectively. For both these samples, the reaction kinetics is likely limited by the small numbers of active site (edges), where adsorption of H^+ takes place, as indicated by the large Tafel slope approaching the theoretical value of 120 mV/dec.[52,54] Moreover, pure $MoTe_2$

exhibits a quite good Tafel slope of 84 mV/dec, low enough to suggest the existence of a mixed mechanism.

Interestingly, MoTe$_2$ shows better activity than MoSe$_2$, with respect to all considered benchmark. This result contradicts what is mostly reported in the literature, where 2H-MoSe$_2$ is generally considered one of the best TMC catalysts.[55] Theoretical investigations suggest that the active sites are Mo or Se edges, most likely through a Volmer-Tafel mechanism.[56,57] However, defects such as Se vacancies are excellent catalytic centers, in this case a Volmer-Heyvrosky mechanism is favored.[56] Experimentally, Tafel slopes as low as 76 mV/dec, and 65 mV/dec for 2H- and 1T-MoSe$_2$ were reported. On the contrary, the 2H-MoTe$_2$ is mainly reported to be poorly active. A very complete and accurate study on bulk 2H-MoTe$_2$ single crystal has showed that this material is almost completely inert and only the 1T phase shows activity, which however is due to a Peierls type transition induced by the adsorption of hydrogen.[27] Similarly, a comparative work on exfoliated 2H nanosheets indicates that MoSe$_2$ is better performing than MoTe$_2$.[53] Besides, it was recently reported that the Tafel slope of 2H bulk materials is around 150 mV/dec,[29] however, chemically exfoliated 1T nanosheets may exhibit a much lower value: 57 mV/dec.[29] Theoretical calculations suggest that tellurides should have a lower activity then sulfides and selenides, in fact the Gibbs free energy of adsorption of hydrogen on MoTe$_2$ metallic edges is calculated to be 0.57 eV[29] or 0.77 eV,[27] whereas is almost thermoneutral for MoSe$_2$ edges and defects.[56] It has to be noted however that in the present case the amount of edges and defects is quite low in our model ultrathin films

and their electrochemistry is ruled mainly by the intrinsic activity of the basal plane. The special chemical activity observed in $MoTe_2$ compared to $MoSe_2$ can be likely associated with the presence of MTB that improve the electronic transfer capability of the films.[45,58] As a matter of fact, these boundaries are much 6-7 times denser in $MoTe_2$ than $MoSe_2$ (see **Figure S2** supporting information). Such extended linear defects therefore impart the otherwise scarcely reactive $2H-MoTe_2$ phase with a new high activity, which is even better than the basal plane of $MoSe_2$. It is worth noting that both selenotellurides exhibit better performance than the two pure end members, $MoSe_2$ (-0.62 V) and $MoTe_2$ (-0.51 V). The dependence of the HER activity on the composition though is quite complex and not simply related with the concentration of the chalcogenides, probably because several factors are at play. The rigid shift of the BE positions in the photoemission peak of Se and Mo in $MoSe_2$ vs $MoSe_{2-x}Te_x$, but without the formation of different chemically shifted components would suggest that the Se atoms are atomically dispersed into a matrix of $MoTe_2$, which is little perturbed since Te and Mo photoemission peaks nicely match with those of pure $MoTe_2$. Recent theoretical calculations have shown that Mo selenotellurides are thermodynamically stable compounds with smoothly varying electronic properties with respect to pure family end members.[30] Besides, it has to be mentioned that the presence of Se is also beneficial for the resistance to oxidation of the materials: tellurides are almost immediately oxidized when exposed to air on the contrary selenides exhibit a better resistance.

In order to get insight into HER at the microscopic level, we carried out first-principles calculations as described below. We first studied the adsorption of H atoms on pristine 2H-MoTe$_2$. We considered high-symmetry positions such as on top of Te and Mo atoms, hollow-site and interstitial position, see **Figure. 4**(a). Surprisingly, we found that in the pristine MoTe$_2$ sheet H atoms prefer to occupy the interstitial positions within the Mo atom plane, see the inset in Figure. 4(a). This is fundamentally different to the case of MoS$_2$, where, according to our calculations, the interstitial position is energetically unfavorable and H atoms prefer to be on top of S atoms, which is associated with the larger unit cell size of MoTe$_2$ as compared to MoS$_2$. Other sites proved to be considerably higher in energy, being in agreement with previous calculations for the pristine 2H-MoTe$_2$ system.[27]

Having analyzed adsorption on pristine 2H MoTe$_2$ sheet, we studied the adsorption of hydrogen on Te vacancies and MTBs. We found that the interaction of H atoms with vacancies is very strong, 0.43 eV per H atom is released when H$_2$ molecule is broken and H atoms are adsorbed on the reactive dangling bonds. Zero-point vibrations and entropy contribute about 0.2 eV, so that Gibbs energy difference ΔG_H is -0.23 eV, Figure. 4(b). Vacancies appear to be very promising defects for HER, but their concentration was rather small in our pristine samples as suggested by XPS and STM data. However, anion vacancies are formed as a consequence of mild Ar$^+$ sputtering, and indeed sample S2 after such treatment exhibits a clear increase of the catalytic activity, both in terms of onset potential and Tafel slope.

Adsorption of H atoms onto interstitial positions next to MTBs also proved to be preferable with energy gain of 0.4 eV as compared to the pristine system. Calculations indicated that the energy gain remains even for a relatively high concentration of H atoms (one H atom per MTB unit cell), and overall H atoms prefer to occupy nearby interstitial positions, which may facilitate hydrogen evolution through a Tafel desorption mechanism. We note that local charge and stress present in the systems with MTBs can further decrease ΔG_H. Moreover, our calculations for finite-length triangular MTB showed that ΔG_H decreases by 0.1 eV at the corners or vertices where MTBs meet (see **Figure S3** and Supplementary Information for details). Finally, we studied the adsorption of H near Se impurities in the substitutional positions in the otherwise pristine system and close to MTBs. We did not find substantial differences with respect to the case of 2H $MoTe_2$ sheets without impurities. Se impurities may still have an indirect influence on HER by affecting the concentration of MTBs and electronic properties of the material, e.g., it band gap and most probably imparting a better resistance to oxidation, but are not *per se* better catalytic sites than Te atoms.[30]

The unavoidable presence of oxides in the films strongly influences the HER performance. MoO_3 and TeO_2 oxides are normally considered catalytically inactive,[59] although recently, it was suggested that oxidized $MoTe_2$ still maintains some catalytic activity.[29] As shown in **Figure S4a**, the overpotential becomes smaller when the oxide amount decreases. Moreover, the pre-waves observed on the first polarization curve of sample S2 indicate the presence of reduction and dissolution processes (see Figure 3d), which eventually lead to a slight

12

improvement of the HER performance. These pre-waves can be connected to decomposition/dissolution of the MoO_3 and TeO_2 from the surface,[29] which exposes active sites for the hydrogen evolution. This hypothesis is confirmed by the photoemission spectra taken after HER measurements shown in Figure S4. The deconvolution of Mo3d, Te3d photoemission spectra of sample S2 after HER, indicates an increase of 2H phase from 64.9% to 70.1% and from 72.7% to 76% for Mo and Te, respectively, whereas the oxide component is reduced from 35.1% to 29.9% and from 27.3% to 24.0% for Mo and Te, respectively.

In conclusion, we have outlined a new strategy for the improvement of the electrochemical performance of TMDs, which is due to special metallic twin boundaries that are obtained when these materials are deposited by MBE as thin films. This novel strategy is similarly to the exploitation of 1T polymorphs in WS_2 and MoS_2 that have metallic properties and therefore show HER activity not only at edges, but also in the basal plane. However, these phases are metastable and inevitably degrade with time. Metallic twin boundaries on the contrary, are the most thermodynamically stable defects and therefore are expected to provide materials with better stability. These defects can be observed in several type of chalcogenides and can be obtained using several approaches (direct synthesis by MBE or electron beam bombardment or vacuum annealing)[44,58] Their special electronic structure and versatile geometry made them quite interesting to impart TMCs at the nano- or macro-scale,[60] with special functional properties such as metallic conductions and unprecedented chemical activity. Therefore, the

control of MTB offers a quite versatile tool for the development of advanced multifunctional materials.

Experimental Section

Sample growth and characterization: Thin films of transition metal dichalcogenides TMDC based on Mo, Se and Te with different composition have been grown by MBE on HOPG under UHV conditions (growth chamber pressure $1x10^{-9}$ mbar) as reported in details in some previous works.[35, 36, 37, 39] A freshly exfoliated HOPG sample was outgassed for 4h at 300°C and then exposed to a flux of metal and chalcogen atoms in a 1:10 ratio. Mo was evaporated from a home-built water-cooled e-beam evaporator; atomic selenium was supplied by a valved, hot-wall selenium cracker source, while tellurium was evaporated from a water-cooled effusion cell. The growth rate was about 0.75 monolayer per hour at a substrate temperature of 300°C. The STM measurements were acquired in situ with an Omicron STM 1 instrument. Electrochemically etched W-tips were used. The STM was used for imaging and local I–V spectroscopy. dI/dV derivatives were obtained numerically.

The valence band photoemission measurements were acquired using a VUV He discharge lamp and an Omicron Sphere II electron analyzer, installed in an UHV analysis systems connected via vacuum transfer to the MBE growth chamber.

The chemical composition before and after electrochemical work was determined by XPS. The measurements were carried out in a custom-designed UHV system equipped with an EA 125 Omicron electron analyzer ending with a five channeltron detector, working at a base pressure

of 10^{-10} mbar. The photoemission spectra were collected at room temperature using the Al Kα line (hν=1486.6 eV) of a non-monochromatized dual-anode DAR400 X-ray source. High resolution spectra were acquired using 0.1 eV energy steps, 0.5 s collection time, and 20 eV pass energy. The identification of chemically shifted components in the Te 3d, Mo 3d and Se 3d photoemission lines was performed by Voigt function and subtracting a Shirley background using the KolXPD software.

Electrochemical measurements. The electrochemical HER measurements were carried out in a standard three-electrode electrochemical cell with an Autolab PGSTAT302 (Ecochemie) potentiostat. A carbon rod was used as a counter electrode, whereas an Ag/AgCl$_{(3M\ KCl)}$ electrode, calibrated with respect to the reversible hydrogen electrode (RHE), was used as reference electrode. All potentials reported in the text and figures are referred to the (RHE) and corrected according to the equation: E(RHE)=E(Ag/AgCl) + 0.272 V. The EC experiments were carried out in 0.5 M H_2SO_4 solution prepared from high-purity reagents (Sigma-Aldrich) and ultrapure Mill-Q water with a resistivity of 18.2 MΩ.

First-principles calculations. First-principles calculations were carried out in the framework of the spin-polarized density functional theory and using projector-augmented waves and PBE exchange-correlation functional as implemented in the VASP code [61]. The pristine system was modeled as a 6x6 supercells, with the Brillouin zone sampled using a (4x4x1) mesh. Calculations with MTBs were carried for a ribbon geometry with 72 atoms in the supercell or for finite triangular MTBs (corresponding to 5 additional Mo atoms) embedded into a 10x10

supercell. Gibbs free energy of formation is evaluated by adding zero-point energy and

entropy corrections (see SI) to the calculated formation energies, as in Ref. [56].

Supporting Information
Supporting Information is available from the Wiley Online Library or from the author.

References

[1]   Y. Zheng, Y. Jiao, S. Qiao, A. Vasileff, *Angew. Chemie Int. Ed.* **2018**, DOI 10.1002/anie.201710556
[2]   S. Trasatti, *J. Electroanal. Chem.* **1972**, *39*, 163.
[3]   Y. Zheng, Y. Jiao, Y. Zhu, L. H. Li, Y. Han, Y. Chen, M. Jaroniec, S.-Z. Qiao *J. Am. Chem. Soc.* **2016**, 138, 16174-16181
[4]   S. Anantharaj, S. R. Ede, K. Sakthikumar, K. Karthick, S. Mishra, S. Kundu, *ACS Catal.* **2016**, *6*, 8069.
[5]   J. Hu, C. Zhang, X. Meng, H. Lin, C. Hu, X. Long, S. Yang, *J. Mater. Chem. A* **2017**, *5*, 5995.
[6]   B. Hinnemann, P. G. Moses, J. Bonde, K. P. Jørgensen, J. H. Nielsen, S. Horch, I. Chorkendorff, J. K. Nørskov, *J. Am. Chem. Soc.* **2005**, *127*, 5308.
[7]   M. A. Lukowski, A. S. Daniel, F. Meng, A. Forticaux, L. Li, S. Jin, *J. Am. Chem. Soc.* **2013**, *135*, 10274.
[8]   D. Voiry, H. Yamaguchi, J. Li, R. Silva, D. C. B. Alves, T. Fujita, M. Chen, T. Asefa, V. B. Shenoy, G. Eda, M. Chhowalla, *Nat. Mater.* **2013**, *12*, 850.

[9]   D. Kong, H. Wang, J. J. Cha, M. Pasta, K. J. Koski, J. Yao, Y. Cui, *Nano Lett.* **2013**, *13*, 1341.

[10]   X. Zheng, J. Xu, K. Yan, H. Wang, Z. Wang, S. Yang, *Chem. Mater.* **2014**, *26*, 2344.

[11]   F. Carraro, L. Calvillo, M. Cattelan, M. Favaro, M. Righetto, S. Nappini, I. Píš, V. Celorrio, D. J. Fermín, A. Martucci, S. Agnoli, G. Granozzi, *ACS Appl. Mater. Interfaces* **2015**, *7*, 25685.

[12]   J. Shi, D. Ma, G. F. Han, Y. Zhang, Q. Ji, T. Gao, J. Sun, X. Song, C. Li, Y. Zhang, X. Y. Lang, Y. Zhang, Z. Liu, *ACS Nano* **2014**, *8*, 10196.

[13]   C. Du, H. Huang, J. Jian, Y. Wu, M. Shang, W. Song, *Appl. Catal. A Gen.* **2017**, *538*, 1.

[14]   G. Ye, Y. Gong, J. Lin, B. Li, Y. He, S. T. Pantelides, W. Zhou, R. Vajtai, P. M. Ajayan, *Nano Lett.* **2016**, *16*, 1097.

[15]   Y. Ouyang, C. Ling, Q. Chen, Z. Wang, L. Shi, J. Wang, *Chem. Mater.* **2016**, *28*, 4390.

[16]   H. Li, C. Tsai, A. L. Koh, L. Cai, A. W. Contryman, A. H. Fragapane, J. Zhao, H. S. Han, H. C. Manoharan, F. Abild-Pedersen, J. K. Nørskov, X. Zheng, *Nat. Mater.* **2015**, *15*, 48.

[17]   J. Kibsgaard, Z. Chen, B. N. Reinecke, T. F. Jaramillo, *Nat. Mater.* **2012**, *11*, 963.

[18]   S. Jiang, Z. Zhang, N. Zhang, Y. Huan, Y. Gong, M. Sun, J. Shi, C. Xie, P. Yang, Q. Fang, H. Li, L. Tong, D. Xie, L. Gu, P. Liu, Y. Zhang, *Nano Res.* **2017**, DOI 10.1007/s12274-017-1796-8.

[19]   H. Li, M. Du, M. J. Mleczko, A. L. Koh, Y. Nishi, E. Pop, A. J. Bard, X. Zheng, *J. Am. Chem. Soc.* **2016**, *138*, 5123.

[20]   Y. Chen, K. Yang, B. Jiang, J. Li, M. Zeng, L. Fu, *J. Mater. Chem. A* **2017**, *5*, 8187.

[21]   C. Ruppert, O. B. Aslan, T. F. Heinz, *Nano Lett.* **2014**, *14*, 6231.

[22]   Y. Qi, P. G. Naumov, M. N. Ali, C. R. Rajamathi, W. Schnelle, O. Barkalov, M. Hanfland, S. C. Wu, C. Shekhar, Y. Sun, V. Süß, M. Schmidt, U. Schwarz, E. Pippel, P. Werner, R. Hillebrand, T. Förster, E. Kampert, S. Parkin, R. J. Cava, C. Felser, B. Yan, S. A. Medvedev, *Nat. Commun.* **2016**, *7*, 11038.

[23]   L. Huang, T. M. McCormick, M. Ochi, Z. Zhao, M. T. Suzuki, R. Arita, Y. Wu, D. Mou, H. Cao, J. Yan, N. Trivedi, A. Kaminski, *Nat. Mater.* **2016**, *15*, 1155.

[24]   H. J. Seo, W. Jeong, S. Lee, G. D. Moon, *Nanoscale* **2018**, DOI 10.1039/C8NR01429A

[25]   A. Politano, G. Chiarello, C.-N. Kuo, C. S. Lue, R. Edla, P. Torelli, V. Pellegrini, D. W. Boukhvalov, *Adv. Funct. Mater.* **2018**, 1706504.

[26]   M. Zeng, Y. Xiao, J. Liu, K. Yang, L. Fu *Chem. Rev.*, **2018** Article ASAP **DOI:** 10.1021/acs.chemrev.7b00633

[27]   J. Seok, J. H. Lee, S. Cho, B. Ji, H. W. Kim, M. Kwon, D. Kim, Y. M. Kim, S. H. Oh, S. W. Kim, Y. H. Lee, Y. W. Son, H. Yang, *2D Mater.* **2017**, *4*, 025061.

[28] Y. Zhou, L. Jia, Q. Feng, T. Wang, X. Li, C. Wang, *Electrochim. Acta* **2017**, *229*, 121.

[29] J. Luxa, P. Vosecký, V. Mazánek, D. Sedmidubský, M. Pumera, P. Lazar, Z. Sofer, *ACS Catal.* **2017**, *7*, 5706.

[30] H. P. Komsa, A. V Krasheninnikov, *J. Phys. Chem. Lett.* **2012**, *3*, 3652.

[31] L. Yang, W. Wang, Q. Fu, J. Zhang, B. Xiang, *Electrochim. Acta* **2015**, *185*, 236.

[32] L. Yang, Q. Fu, W. Wang, J. Huang, J. Huang, J. Zhang, B. Xiang, *Nanoscale* **2015**, *7*, 10490.

[33] Q. Gong, L. Cheng, C. Liu, M. Zhang, Q. Feng, H. Ye, M. Zeng, L. Xie, Z. Liu, Y. Li, *ACS Catal.* **2015**, *5*, 2213.

[34] Q. Fu, L. Yang, W. Wang, A. Han, J. Huang, P. Du, Z. Fan, J. Zhang, B. Xiang, *Adv. Mater.* **2015**, *27*, 4732.

[35] K. Xu, F. Wang, Z. Wang, X. Zhan, Q. Wang, Z. Cheng, M. Safdar, J. He, *ACS Nano* **2014**, *8*, 8468.

[36] S. Hussain, K. Akbar, D. Vikraman, K. Karuppasamy, H.-S. Kim, S.-H. Chun, J. Jung, *Inorg. Chem. Front.* **2017**, DOI 10.1039/C7QI00457E.

[37] X. Xu, Y. Ge, M. Wang, Z. Zhang, P. Dong, R. Baines, M. Ye, J. Shen, *ACS Appl. Mater. Interfaces* **2016**, *8*, 18036.

[38] X. Chen, Y. Qiu, G. Liu, W. Zheng, W. Feng, F. Gao, W. Cao, Y. Fu, W. Hu, P. Hu, *J. Mater. Chem. A* **2017**, *5*, 11357.

[39] J. Miao, F.-X. Xiao, H. B. Yang, S. Y. Khoo, J. Chen, Z. Fan, Y.-Y. Hsu, H. M. Chen, H. Zhang, B. Liu, *Sci. Adv.* **2015**, *1*, e1500259.

[40] H. C. Diaz, Y. Ma, S. Kolekar, J. Avila, C. Chen, M. C. Asensio, M. Batzill, *2D Mater.* **2017**, *4*, 25094.

[41] Y. Ma, S. Kolekar, H. Coy Diaz, J. Aprojanz, I. Miccoli, C. Tegenkamp, M. Batzill, *ACS Nano* **2017**, *11*, 5130.

[42] H. C. Diaz, Y. Ma, R. Chaghi, M. Batzill, *Appl. Phys. Lett.* **2016**, *108*, 191606.

[43] H. Liu, L. Jiao, F. Yang, Y. Cai, X. Wu, W. Ho, C. Gao, J. Jia, N. Wang, H. Fan, W. Yao, M. Xie, *Phys. Rev. Lett.* **2014**, *113*, 066105.

[44] H. Zhu, Q. Wang, L. Cheng, R. Addou, J. Kim, M. J. Kim, R. M. Wallace *ACS Nano* **2017** *11*, 11005-11014

[45] H. C. Diaz, R. Chaghi, Y. Ma, M. Batzill, *2D Mater.* **2015**, *2*, 044010.

[46] S. Vishwanath, X. Liu, S. Rouvimov, P. C. Mende, A. Azcatl, S. McDonnell, R. M. Wallace, R. M. Feenstra, J. K. Furdyna, D. Jena, H. Grace Xing, *2D Mater.* **2015**, *2*, 24007.

[47] J. G. Choi, L. T. Thompson, *Appl. Surf. Sci.* **1996**, *93*, 143.

[48] J. . Bernède, C. Amory, L. Assmann, M. Spiesser, *Appl. Surf. Sci.* **2003**, *219*, 238.

[49] Y. A. Teterin, V. I. Nefedov, M. F. Churbanov, A. Y. Teterin, K. I. Maslakov, E. V. Zorin, *Inorg. Mater.* **2007**, *43*, 888.

[50] T. Schroeder, J. Zegenhagen, N. Magg, B. Immaraporn, H. J. Freund, *Surf. Sci.* **2004**, *552*, 85.

[51]   A. Y. S. Eng, A. Ambrosi, Z. Sofer, P. Šimek, M. Pumera, *ACS Nano* **2014**, *8*, 12185.
[52]   J. Benson, M. Li, S. Wang, P. Wang, P. Papakonstantinou, *ACS Appl. Mater. Interfaces* **2015**, *7*, 14113.
[53]   Z. Gholamvand, D. McAteer, C. Backes, N. McEvoy, A. Harvey, N. C. Berner, D. Hanlon, C. Bradley, I. Godwin, A. Rovetta, M. E. G. Lyons, G. S. Duesberg, J. N. Coleman, *Nanoscale* **2016**, *8*, 5737.
[54]   J. D. Benck, T. R. Hellstern, J. Kibsgaard, P. Chakthranont, T. F. Jaramillo, *ACS Catal.* **2014**, *4*, 3957.
[55]   X. Chia, A. Y. S. Eng, A. Ambrosi, S. M. Tan, M. Pumera, *Chem. Rev.* **2015**, *115*, 11941.
[56]   H. Shu, D. Zhou, F. Li, D. Cao, X. Chen, *ACS Appl. Mater. Interfaces* 2017 9 42688
[57]   C. Tsai, K. Chan, F. Abild-Pedersen, J. K. Nørskov, *Phys. Chem. Chem. Phys.* **2014**, *16*, 13156.
[58]   H.-P. Komsa, A. V. Krasheninnikov *Adv. Electron.Mater.* 2017, 3, 1600468
[59]   D. R. Cummins, U. Martinez, A. Sherehiy, R. Kappera, A. Martinez-Garcia, R. K. Schulze, J. Jasinski, J. Zhang, R. K. Gupta, J. Lou, M. Chhowalla, G. Sumanasekera, A. D. Mohite, M. K. Sunkara, G. Gupta, *Nat. Commun.* **2016**, *7*, 11857.
[60]   J. Chen, G. Wang, Y. Tang, H. Tian, J. Xu, X. Dai, H. Xu, J: Jia, W. Ho, M. Xi*e ACS Nano*, **2017**, *11*, 3282–3288
[61] G. Kresse, J. Hafner, Phys. Rev. B 1993, *47*, 558 - 561; G. Kresse, J. Hafner Phys. Rev. B 1994, *49*, 14251- 14269.
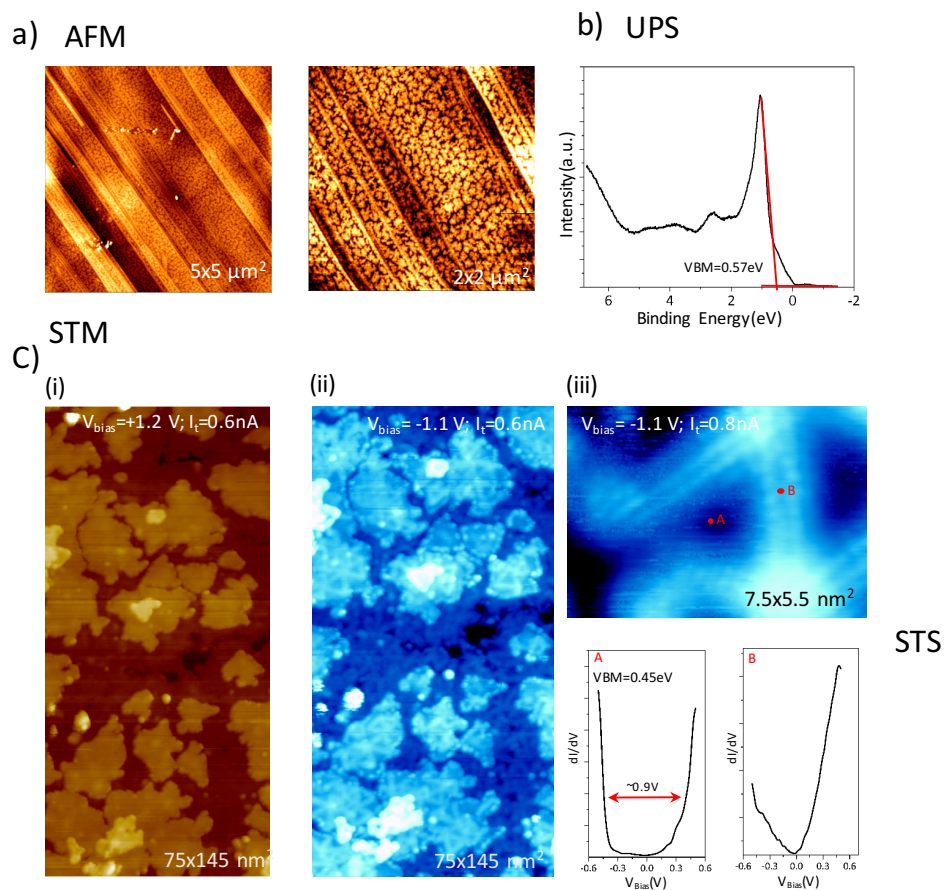
Figure 1: Characterization of the MoSe$_{0.3}$Te$_{1.7}$ film grown on HOPG by *ex-situ* atomic force microscopy (AFM) (a), *in-situ* ultra violet photoemission spectroscopy (UPS) (b), and *in-situ* scanning tunneling microscopy/spectroscopy (STM/S) (c). Bias dependent STM images are shown in (c) for filled states at +1.2 V bias voltage in (i) and empty states at -1.2 V in (ii). In (iii) a zoom in of the defects structure is reported together with STS spectra taken on the "A" and "B" spots.
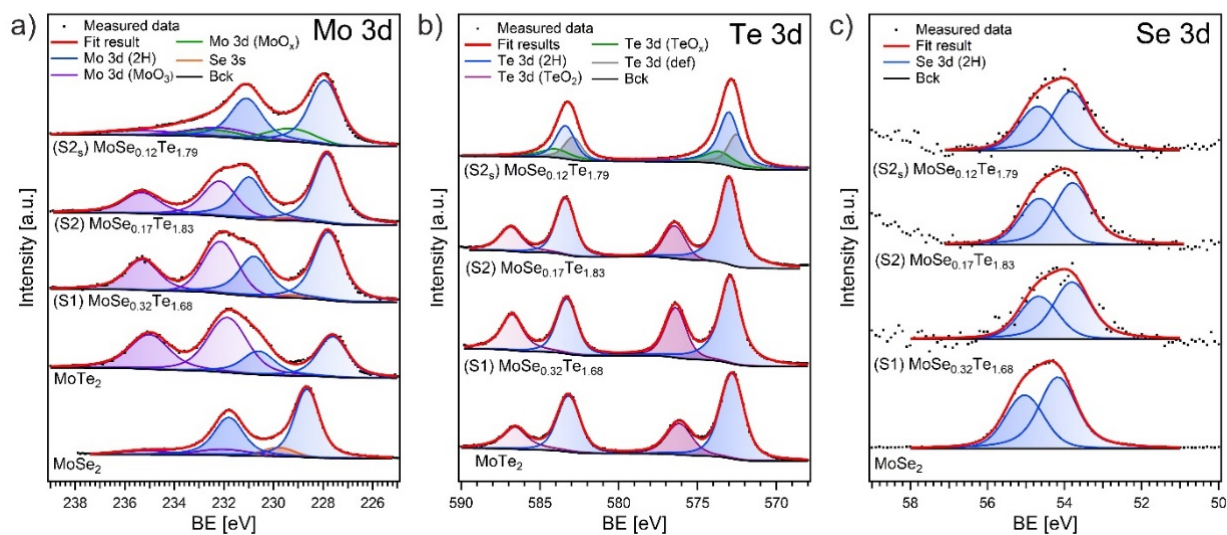
Figure 2. High resolution core-level XPS spectra of (a) Mo 3d, (b) Te 3d and (c) Se 3d of metal dichalcogenide thin films before electrochemical measurements.
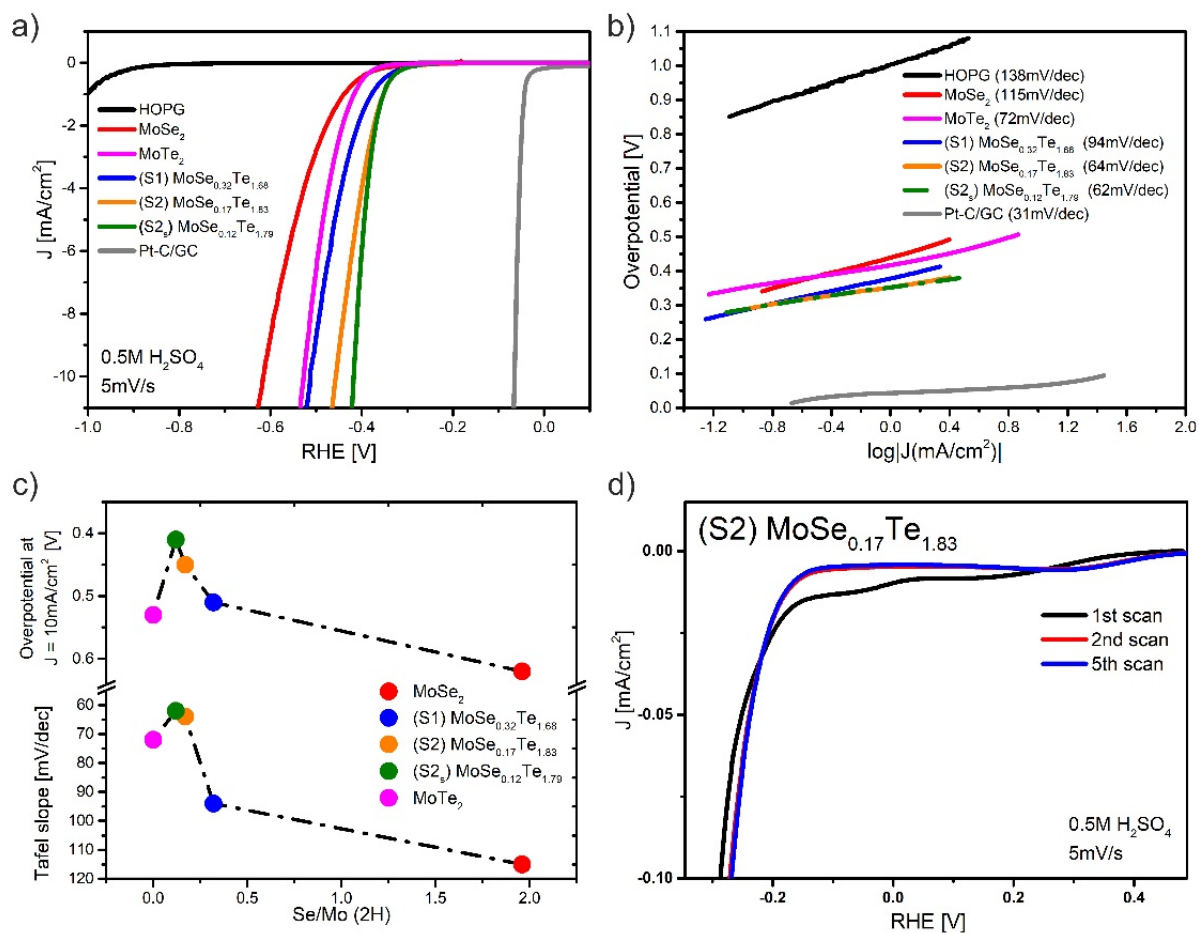
Figure 3. Electrochemical activity of the hydrogen evolution reaction (HER) on metal dichalcogenide catalysts. (a) HER polarization curves, at a scan rate of 5 mV/s, in 0.5 M H_2SO_4; (b) Tafel plot for the HER. (c) Activity volcano plot for the HER showing the overpotentials (a) at current density of 10 mA/cm^{-2} and Tafel slope (b) as a function of Se/Mo (2H) ratio. (d) Sequence of polarization curves for S2.
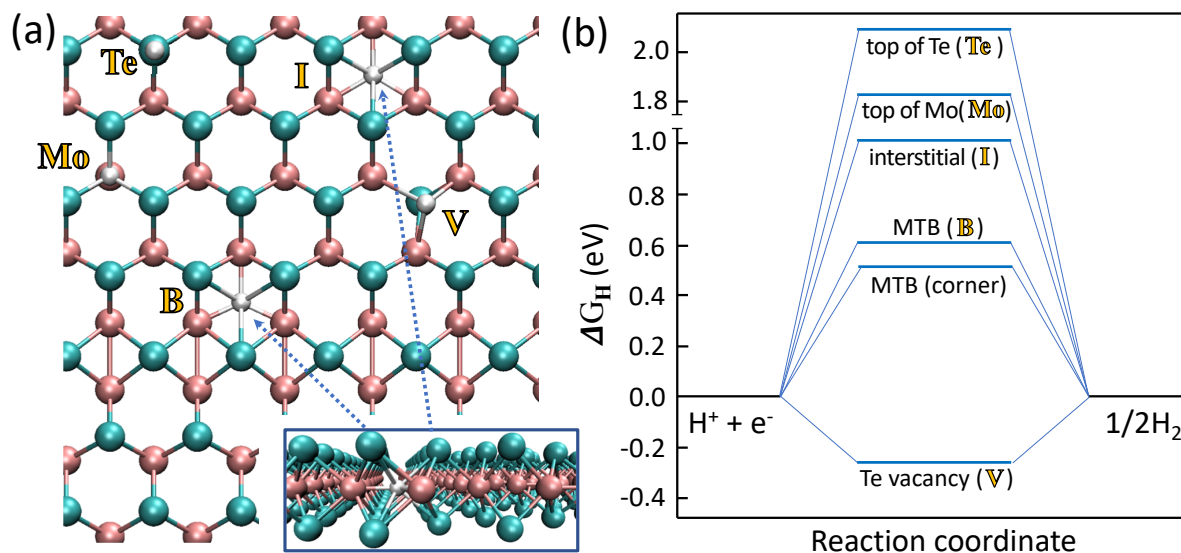
Figure 4. (a) Atomic structure of 2H MoTe$_2$ with adsorbed hydrogen atoms, as revealed by DFT calculations. Pink balls represent Mo atoms, cyan Te atoms, and small white balls H atoms. Several high-symmetry adsorption positions are indicated: on top of Te (Te), on top of Mo (Mo), onto Te single vacancy (V), interstitial position (I) and interstitial position next to mirror twin boundary (B). Note that for the latter two positions H atom is within the Mo atom plane, as evident from the inset in panel (a) showing a side view of the system. (b) Gibbs energy diagram for various adsorption sites. (c) Volcano plot of the exchange current density i_0 versus ΔG_H.

Table 1. Tabulated chalcogenide-to-metal ratios based on high resolution X-ray photoelectron spectroscopy, with the percentage of chemically shifted components of Mo and Te after deconvolution of the core level spectra.

	2H Te/Mo	2H Se/Mo	2H Mo (at. %)	MoO$_3$ (at. %)	MoO$_x$ (at. %)	2H Te (at. %)	TeO$_2$ (at. %)	TeO$_x$ (at. %)	Te$_{def}$ (at. %)
MoSe$_2$	-	1.96	92.2	7.8	-	-	-	-	-
MoTe$_2$	2.03	-	37.4	62.6	--	68.5	31.5	-	-
(S1) Mo Se$_{0.32}$Te$_{1.68}$	1.68	0.32	56.1	43.9	-	61.1	38.9	-	-

(S2) Mo Se$_{0.17}$Te$_{1.83}$	1.83	0.17	62.3	37.7	-	71.9	28.1	-	-
(S2$_s$) Mo Se$_{0.12}$Te$_{1.79}$	1.79	0.12	64.4	19.4	16.2	54.1	-	19.5	26.4

Table 2. Tabulated onset potential, overpotential at 10 ma/cm^2 and Tafel slopes for the different samples.

|	Onset potential vs RHE [V]	Over potential at J = 10mA cm^{-2} vs RHE [V]	Tafel slope [mV/dec]
MoSe$_2$	-0.29	0.62	115
MoTe$_2$	-0.25	0.53	72
(S1) Mo Se$_{0.32}$Te$_{1.68}$	-0.24	0.51	94
(S2) Mo Se$_{0.17}$Te$_{1.83}$	-0.19	0.45	64
(S2$_s$) Mo Se$_{0.12}$Te$_{1.79}$	-0.18	0.41	62

The table of contents

The HER activity of the normally inert basal plane of MoTe$_2$ can be boosted be growing ultrathin films characterized by a high density of metallic twin boundaries and by exchanging some Te ions with Se.

Keyword hydrogen evolution reaction, electrocatalysis, transition metal dichalcogenides

*Tomasz Kosmala, Horacio Coy Diaz, Hannu-Pekka Komsa, Yujing Ma, Arkady V. Krasheninnikov Matthias Batzill, Stefano Agnoli ***

Metallic twin boundaries and anion substitution boost the hydrogen evolution reaction on the basal plane of molybdenum selenotellurides
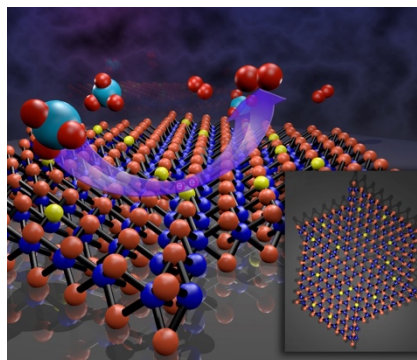
Supporting Information

Metallic twin boundaries and anion substitution boost the hydrogen evolution reaction on the basal plane of molybdenum selenotellurides

*Tomasz Kosmala, Horacio Coy Diaz, Hannu-Pekka Komsa, Yujing Ma, Arkady V. Krasheninnikov Matthias Batzill, Stefano Agnoli ***
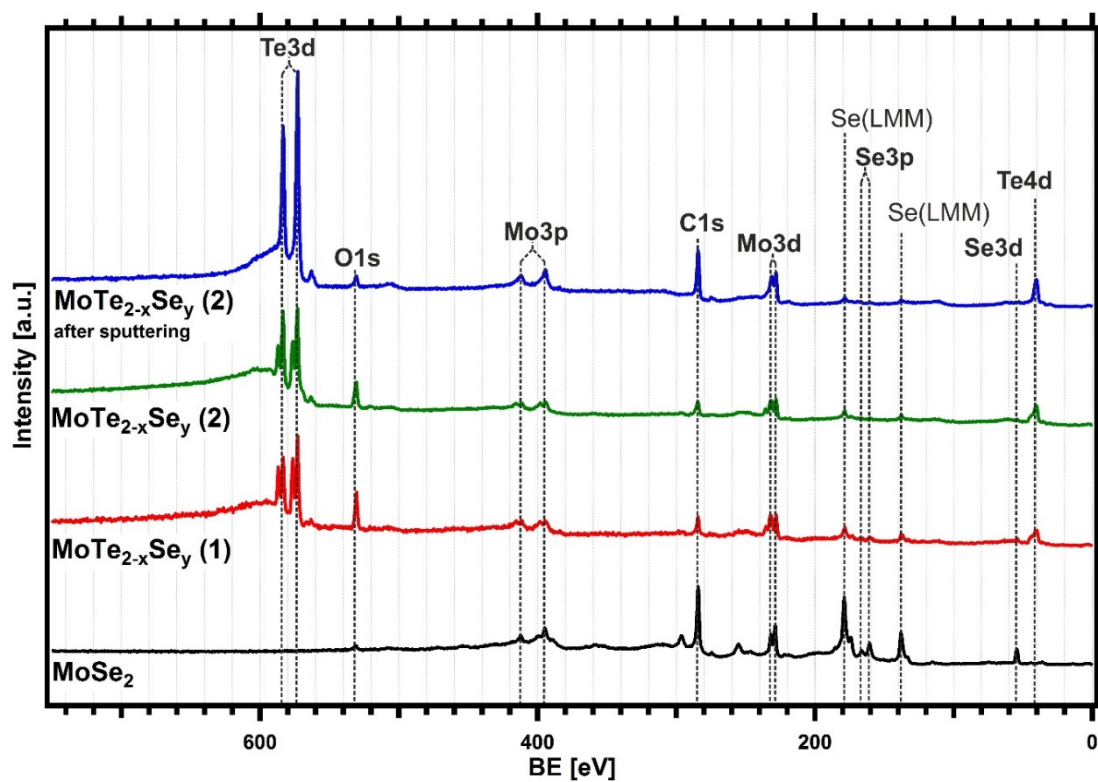
XPS Characterization

Figure S1. XPS survey spectra of TMDs catalysis in prior to EC measurements.

Scanning Tunnelling Microscopy characterization of pure MoSe₂
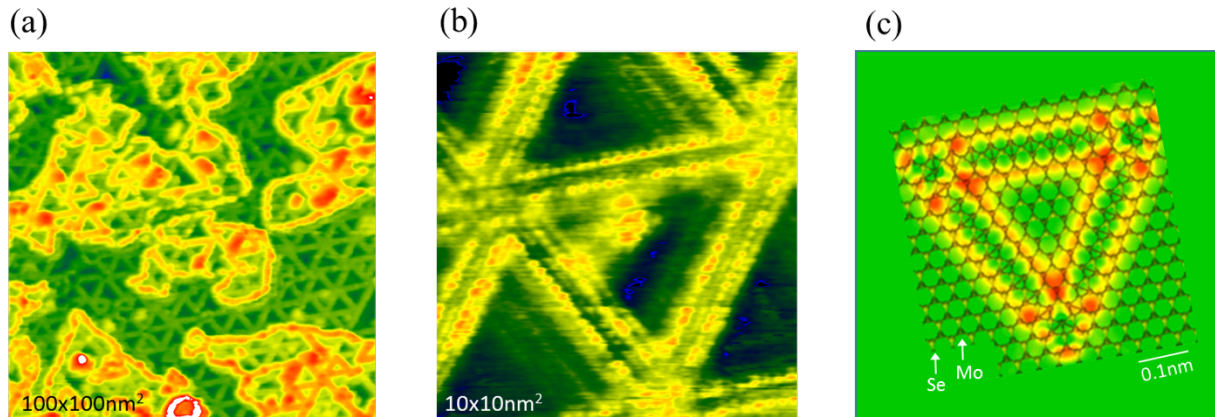

Figure S2. MTBs structure in 1-2 monolayers of MoSe₂ grown by MBE on MoS₂. (a) Large scale STM image shows a dense network of MTBs. (b). High resolution STM image of the MTBS. The MTBs appear as two bright parallel Se –rows. (c) Tersoff-Hamann Simulated STM image of the MTBs

Details of first-principles calculations

To evaluate the Gibbs free energy of formation, we largely follow the approach laid out in Refs. [x,y] with minor modifications. We write the free energy of formation as

$$\Delta_f G = G\left(\text{MoTe}_2 + \text{H}^*\right) - \left[G(\text{MoTe}_2) + \frac{\mu(\text{H}_2)}{2}\right] = \Delta_f E + \mu_{\text{vib}}\left(\text{H}^*\right) - \frac{\mu(\text{H}_2)}{2}$$

where

$$\Delta_f E = E(MoTe_2 + H^*) - [E(MoTe_2) + E(H_2)/2]$$

is the formation energy as obtained using only DFT total energies. For the vibrational free energy contribution, we assume that the vibrations of the host cancel in both systems and vibrational contribution to free energy ($\mu_{\text{vib}} = -kT \ln Z_{vib}$) can be evaluated using only the vibrational modes of the adsorbed H atom, via the partition function:

$$Z_{vib} = \prod_i \frac{e^{-\epsilon_i/2T}}{1 - e^{-\epsilon_i/T}}$$

As in Refs. [x,y], the vibrational energies ($\epsilon_i = \hbar\omega_i$) are evaluated by displacing the adsorbed H atom in x, y, and z directions and fixing all other atoms to their equilibrium positions. Note that μ_{vib} contains zero-point energy (ZPE) of the H atom.

The free energy of H_2 molecule is given as

$$\mu(H_2) = E(H_2) + E_{\text{ZPE}} + \Delta H - TS = E(H_2) - 43.2 \text{ meV}$$

or about 21.6 meV per H atom. For zero-point energy, enthalpy change from 0K to room temperature, and entropy at standard conditions we use experimental values, which may all be obtained from thermochemical tables.

The vibrational energies for H atoms obtained this way are all listed in Table S1. For all systems except the Te vacancy, the degenerate energies correspond to lateral vibrations and the nondegenerate energy to vibrational normal to the $MoTe_2$ layer. As expected, in interstitial site, the lateral energies are higher than normal to the layer due to the neighboring Mo atoms, whereas the opposite is true in adatom sites since H atom is bonded strongly only to the atom directly under it.

Table S1. Vibrational energies of the adsorbed H atoms (in meV).

	ϵ_1	ϵ_2	ϵ_3
Interstitial (pristine)	88.81	115.03	115.33
Interstitial (MTB)	75.25	140.87	143.10
Adatom (Te)	56.63	56.65	233.11
Interstitial (near Se)	75.63	78.70	214.66
Adatom in V_{Te}	46.29	128.23	145.02

The energy contributions calculated from these are collected in Table S2. The final column gives the final correction that needs to be added to the DFT formation energies $\Delta_f E$. It is found to lie close to 0.2 eV in all cases, which can be used to obtain quick estimate for all other cases shown in the SI.

Table S2. Energies contributions and final formation energies at different sites (in eV).

	ZP E	-TS	μ_{vib}	μ_{vib} $+ \mu(H_2)/2$	$\Delta_f E$	$\Delta_f G$
Interstitial (pristine)	0.160	-0.007	0.158	0.180	0.84	1.02
Interstitial (MTB)	0.180	-0.007	0.178	0.200	0.42	0.62
Adatom (Te)	0.173	-0.020	0.167	0.189	1.90	2.09
Interstitial (near Se)	0.184	-0.011	0.182	0.203	1.58	1.78

Adatom in V_{Te}	0.160	-0.015	0.155	0.176	-0.44	-0.26

To validate our computational predictions obtained using the ribbon model, we also performed calculations for H atoms adsorbed close to a (small) triangular MTB loop, or an inversion domain. The model, shown in Fig. S2, contains 5 excess Mo atoms and consequently side of the triangle is about 5 lattice constants. The considered interstitial sites as well as the formation energies are also shown in Fig. S2. The formation energies at the outer edges agree well with the ribbon calculations. On the other hand, the formation energy at the inner corners is lower by about 0.1 eV. Formation energy far from MTB is somewhat lower than in pristine system calculations, which we assign to charge transfer from the H to the MTB. Similar effect was found for the far-from-MTB site in the ribbon calculations.
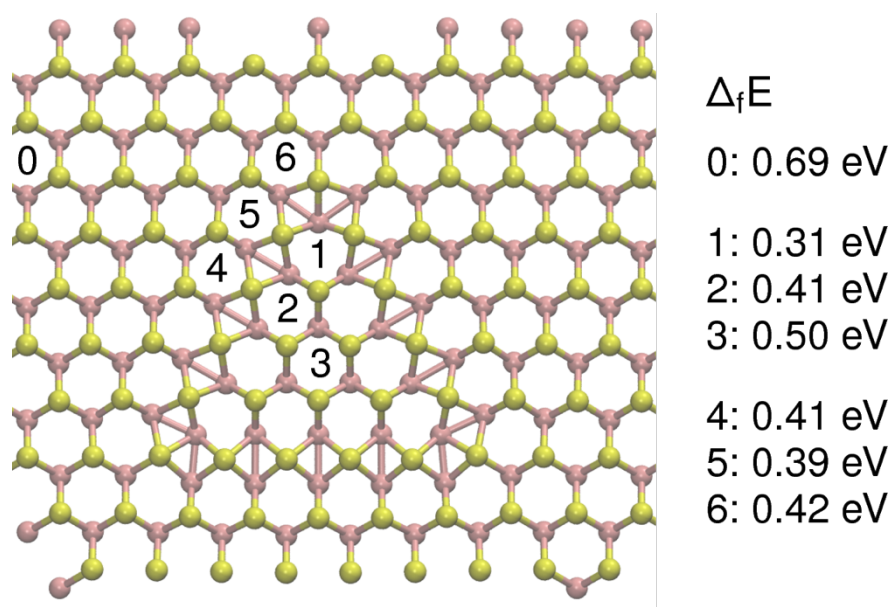

$\Delta_f E$

0: 0.69 eV

1: 0.31 eV
2: 0.41 eV
3: 0.50 eV

4: 0.41 eV
5: 0.39 eV
6: 0.42 eV

Figure S3. Atomic structure of MTB loop of size N=5 embedded within 10x10 supercell of MoTe$_2$. Different interstitial sites for H are indicated in the structure and the corresponding formation energies are given on the right.

Tafel Analysis

The linear portion of the Tafel plots were fitted to the Tafel equation ($\eta = b\log|J| + a$, where η is overpotential, J is the current density, a is exchange current density, and b is the Tafel slope) in order to determine the Tafel slope. A small Tafel slope is highly desirable since it indicates a fast increase of H$_2$ generation rate with the applied overpotential. In general, the HER proceeds through three principal reaction steps in acid media:[4–7]
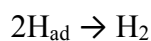
    (1) Volmer adsorption step (Tafel slope 120 mV dec^{-1})

$H_3O^+ + e^- \rightarrow H_{ad} + H_2O$ (1)

    (2) Heyrovsky desorption step (Tafel slope 40 mV dec^{-1})

$H_{ad} + H_3O^+ + e^- \rightarrow H_2 + H_2O$
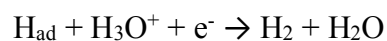
    (3) Tafel desorption step (Tafel slope 30 mV dec^{-1})

$2H_{ad} \rightarrow H_2$

where H$_{ad}$ is the hydrogen adsorption site onto the surface of the catalyst. Experimentally, two-step reaction pathways are generally observed for HER, a Volmer-Heyrovsky (eqs 1 and 2), or a Volmer-Tafel (eqs 1 and 3) type of mechanism.

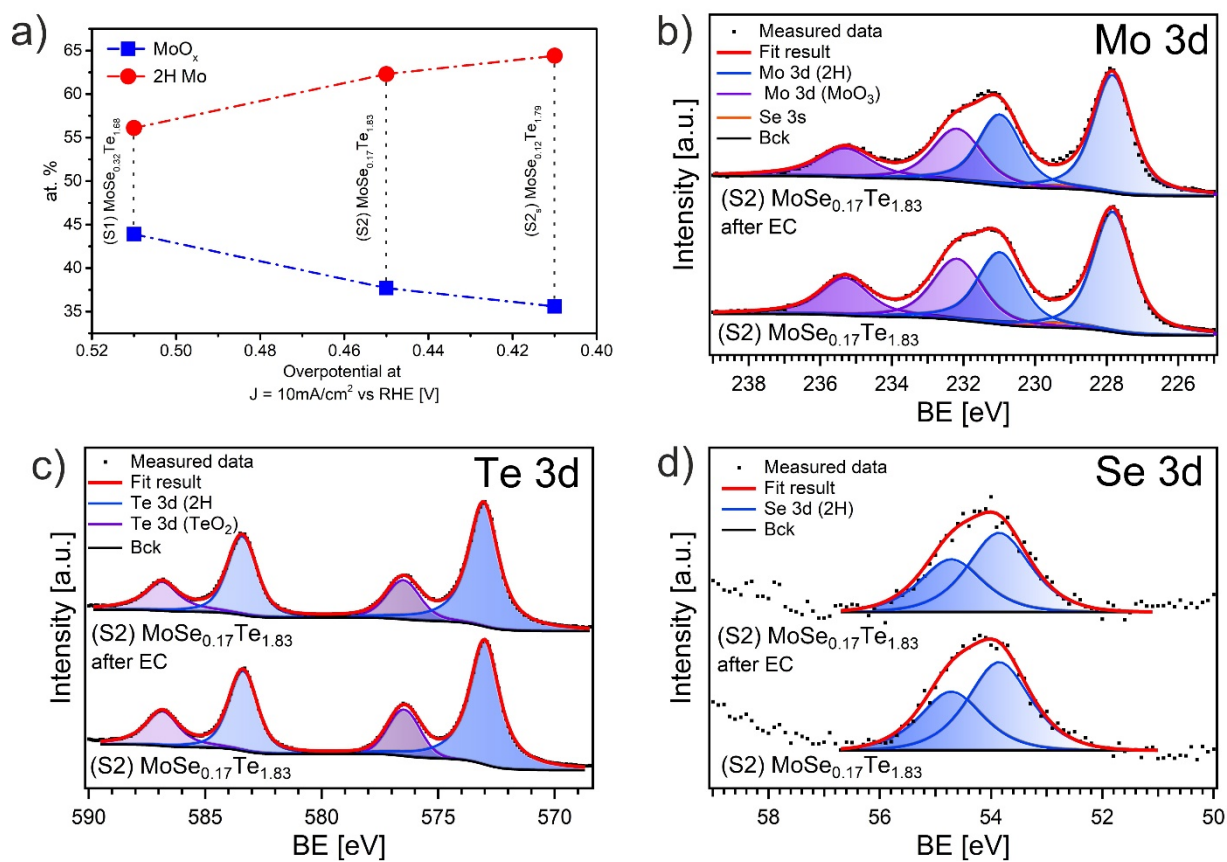**Additional characterization by XPS**

Figure S4. High resolution core-level XPS spectra of Mo3d, Te3d and Se3d of metal dichalcogenide catalysts of MoSe$_2$ and MoTe$_{2-x}$Se$_y$ (2) before and after electrochemical (EC) measurements.

References

[1]   H. J. Seo, W. Jeong, S. Lee, G. D. Moon, *Nanoscale* **2018**, DOI
        10.1039/C8NR01429A.

[2]   A. Politano, G. Chiarello, C.-N. Kuo, C. S. Lue, R. Edla, P. Torelli, V. Pellegrini, D.
        W. Boukhvalov, *Adv. Funct. Mater.* **2018**, 1706504.

[3]   E. Skúlason, V. Tripkovic, M. E. Björketun, S. Gudmundsdóttir, G. Karlberg, J.
        Rossmeisl, T. Bligaard, H. Jónsson, J. K. Nørskov, *J. Phys. Chem. C* **2010**, *114*, 18182.

[4]   S. A. Vilekar, I. Fishtik, R. Datta, *J. Electrochem. Soc.* **2010**, *157*, B1040.

[5]   A. Y. S. Eng, A. Ambrosi, Z. Sofer, P. Šimek, M. Pumera, *ACS Nano* **2014**, *8*, 12185.

[6]   J. Benson, M. Li, S. Wang, P. Wang, P. Papakonstantinou, *ACS Appl. Mater. Interfaces*
        2015, *7*, 14113.